Computational Mechanics manuscript No.
(will be inserted by the editor)

Finite Element Modelling of Internal and Multiple Localized Cracks

Savvas Saloustros · Luca Pelà · Miguel Cervera · Pere Roca

Received: date / Accepted: date

Abstract Tracking algorithms constitute an efficient numerical technique for modelling fracture in quasi-brittle materials. They succeed in representing localized cracks in the numerical model without mesh-induced directional bias. Currently available tracking algorithms have an important limitation: cracking originates either from the boundary of the discretized domain or from predefined "crack-root" elements and then propagates along one orientation. This paper aims to circumvent this drawback by proposing a novel tracking algorithm that can simulate cracking starting at any point of the mesh and propagating along one or two orientations. This enhancement allows the simulation of structural case-studies experiencing multiple cracking. The proposed approach is validated through the simulation of a benchmark example and an experimentally tested structural frame under in-plane loading. Mesh-bias independency of the numerical solution, computational cost and predicted collapse mechanisms with and without the tracking algorithm are discussed.

Savvas Saloustros · Luca Pelà · Miguel Cervera · Pere Roca

Department of Civil and Environmental Engineering
Technical University of Catalonia, UPC-BarcelonaTech
Jordi Girona 1-3, 08034 Barcelona, Spain.

International Center for Numerical Methods in Engineering (CIMNE)
Gran Capità, S/N, 08034 Barcelona, Spain.

E-mail: savvas.saloustros@upc.edu
E-mail: luca.pela@upc.edu
E-mail: miguel.cervera@upc.edu
E-mail: pere.roca.fabregat@upc.edu

Keywords Continuum Damage Mechanics · Crack-Tracking · Damage Localization · Quasi-brittle materials · Shear/Flexural/Tensile Cracks

1 Introduction

Almost half a century after the pioneering works of Ngo & Scordelis [1] and Rashid [2], the numerical simulation of cracking in quasi-brittle materials is still a challenging task. Although a wide range of novel formulations has been proposed in the field of computational failure mechanics, up to date there is no such thing as a panacea for the realistic and efficient numerical analysis of failure in quasi-brittle materials. As a fact, the analyst has to consider at least three aspects before choosing the adequate numerical tool: the realistic numerical modelling of cracking, the accurate simulation of the material behaviour and the bearable computational cost.

Realistic modelling of cracking implies that the location and direction of cracks are not spuriously affected by the used mesh topology. This situation is commonly referred as *mesh-induced directional bias*. The dependency of the numerical simulation to the used mesh is a common limitation of both smeared and discrete crack approaches [3]. This defect has triggered the research, first, on the possible limitations in the numerical discrete problem and, second, on the adequate remedies to overcome them. The proposed solutions depend on the perception of the origin of the numerical problem. Some approaches intervene in the mathematical formulation of the continuum problem, such as gradient-enhanced [4, 5], non-local [6, 7] or micropolar [8, 9] models. Other formulations aim to overcome the error produced by the spatial discretization of the continuum domain, such as

mixed formulations [10], crack-tracking techniques with [11, 12, 13, 14] or without [15, 16, 17] enrichment of the used finite elements or nodes. Finally, another approach reported in the literature bases on the modification of the material model [18]. For a review on the issue the interested reader is referred to [19, 20].

Of equal importance to the numerically objective modelling of cracking, is the accurate simulation of the material behaviour. The description of the mechanical behaviour in quasi-brittle materials necessitates a proper failure criterion and a constitutive law with softening behaviour controlled by the fracture energy. To account for this behaviour various models have been applied for the simulation of quasi-brittle materials based on plasticity [21, 22, 23], continuum damage models [24, 25] or a combination of both [26, 27, 28]. The previous isotropic formulations have been complemented by anisotropic models [29, 30, 31]. In the last years, an increasing effort has been made to develop numerical methods that consider the interaction of components in composite materials (e.g. concrete, masonry). Such methodologies can be based on computational homogenization [32, 33, 34, 35, 36, 37, 38], or on micro-modelling techniques, also known as direct numerical simulations, including all the information about the material's micro-structure [39, 40].

The micro- and multi-scale modelling approaches, even though very sophisticated and characterized by a remarkable level of accuracy, are still hardly applicable to the study of large-scale structural problems experiencing multiple cracking. This is due to the significant computational cost required by these models. As a consequence, the Continuum Finite Element Modelling (also known as macro-modelling) based on the classical smeared crack-approach is still on the foreground of applications in large-scale concrete [41] and masonry structures [42, 43, 44].

The aim of this work is to apply the know-how of objective mesh-localization approaches to the analysis of structures made of quasi-brittle materials that experience multiple cracking. The adopted numerical technique is the classical smeared crack approach enhanced with a local crack-tracking algorithm [16]. This choice is justified by the following reasoning. Firstly, tracking algorithms provide numerical solutions that are free of mesh-induced directional bias [45, 16, 17, 46, 47, 48]. Secondly, the particular tracking algorithm can be effectively combined with constitutive models suitable for quasi-brittle materials, like anisotropic [31, 49] or isotropic ones [26]. Additionally, an important feature of the algorithm is the possibility to define a minimum distance between the discrete cracks. These exclusion zones surrounding a crack render it possible to consider indirectly the size of the material's mesoscale (e.g. masonry units), when the composite is simplified as a homogenized continuum in the numerical simulation. Finally, the overhead in the computational cost is limited, allowing the efficient simulation of multiple cracking problems in large-scale structures.

Up to date approaches using tracking algorithms have focused mostly on cracks nucleating from the boundary of the domain or from pre-existent flaws and propagating in a single orientation (see for instance [46, 47, 50, 51, 52, 53]). This confines the application of tracking algorithms to a very narrow family of structural problems, in which the origin of cracks is either known prior to the analysis, or it is imposed by including material or geometrical perturbations within the analysed numerical domain. Additionally, structural problems with cracking starting from an arbitrary point within the analysed domain and propagating in two opposite orientations have not been addressed.

The main novelty of the present work resides in the enhancement of a crack-tracking algorithm with a technique that allows the initiation and propagation of cracks at any element of the discretized domain. In particular, the proposed methodology extends the use of local crack-tracking algorithms to the simulation of cracking starting from the interior of the discretized domain and propagating along two opposite orientations. This novel contribution to the original methodology [16] makes possible the efficient simulation of localized cracks under shear, flexure and traction, without any *a priori* definition of their location by the analyst. Another original aspect of the proposed method is the identification of the potential crack path prior to the occurrence of the damage, differently from the approach recently proposed in [54].

The paper is structured in the following way. Section 2 presents the underlying continuum damage model. Section 3 outlines the methodology for the simulation of formation and propagation of internal cracking with the use of a crack-tracking algorithm. The proposed numerical strategy is validated with the simulation of a single-crack problem with internal fracture (Brazilian splitting test) and then with the analysis of a complex multi-crack problem (frame wall with one-door opening tested against horizontal loading), see Section 4. Finally, conclusions are summarized in Section 5.

2 Continuum Damage model

In this work, a constitutive model based on the continuum damage mechanics presented in [25] is used for the simulation of fracture. The model benefits from the use of two separate damage scalar indexes to distinguish

between tensile and compressive damage. This is an important characteristic for the simulation of degradation in materials such as concrete and masonry which have quite different capacity under tension and compression. Other local models based on the same concept have been proposed by Lee & Fenves [27], Comi & Perego [55], Wu et al. [28], Pelà et al. [56], Voyiadjis et al. [57], Mazars et al. [58]. He et al. [59] and Pereira et al. [60] have recently proposed nonlocal counterparts of some of the these models.

The constitutive model establishes on the concept of the effective stress tensor $\bar{\boldsymbol{\sigma}}$, which basing on the strain equivalence principle [61] is related to the strain tensor $\boldsymbol{\epsilon}$ according to the following equation

$$\bar{\boldsymbol{\sigma}} = \boldsymbol{C} : \boldsymbol{\epsilon} \tag{1}$$

where $\boldsymbol{C}$ stands for the isotropic linear-elastic constitutive tensor and (:) the tensor product contracted on two indices. Aiming to model a different response under tension and compression, the effective stress is split into a tensile $\bar{\boldsymbol{\sigma}}^+$ and a compressive part $\bar{\boldsymbol{\sigma}}^-$. Such tensors are respectively defined as

$$\bar{\boldsymbol{\sigma}}^+ = \sum_{j=1}^{3} \langle \bar{\sigma}_j \rangle \, \boldsymbol{p_j} \otimes \boldsymbol{p_j} \tag{2}$$

$$\bar{\boldsymbol{\sigma}}^- = \bar{\boldsymbol{\sigma}} - \bar{\boldsymbol{\sigma}}^+ \tag{3}$$

where $\bar{\sigma}_j$ stands for the *j-th* principal stress value from tensor $\bar{\boldsymbol{\sigma}}$ and $\boldsymbol{p_j}$ is the unit vector of the respective principal direction *j*. The symbol $\langle \bullet \rangle$ denotes the Macaulay brackets ($\langle x \rangle = x$, if $x \geq 0$,$\langle x \rangle = 0$, if $x < 0$).

Following that, two internal damage variables are introduced d^+ and d^-, with the first denoting the tensile damage and the second the compressive one. The constitutive relation can be expressed then as

$$\boldsymbol{\sigma} = (1 - d^+)\bar{\boldsymbol{\sigma}}^+ + (1 - d^-)\bar{\boldsymbol{\sigma}}^- \tag{4}$$

Loading, unloading and reloading conditions are distinguished with the use of two scalar positive quantities, one for tension τ^+ and a second for compression τ^-, termed as the equivalent stresses. Their values depend on the stress tensor and the assumed failure criteria. In this work, the failure criterion presented in [26] is used so that the values of the equivalent stresses for tension and compression are

$$\tau^+ = H\left[\bar{\sigma}_{max}\right] \frac{1}{1-\alpha} \left[\sqrt{3\bar{J}_2} + \alpha \bar{I}_1 + \beta \langle \bar{\sigma}_{max} \rangle \right] \frac{f^+}{f^-} \tag{5}$$

$$\tau^- = H\left[-\bar{\sigma}_{min}\right] \frac{1}{1-\alpha} \left[\sqrt{3\bar{J}_2}^- + \alpha \bar{I_1}^- + \beta \langle \bar{\sigma}_{max} \rangle \right] \tag{6}$$

$$\alpha = \frac{\left(f_b^- / f^-\right) - 1}{2\left(f_b^- / f^-\right) - 1} \tag{7}$$

$$\beta = (1-\alpha)\frac{f^-}{f^+} - (1-\alpha) \tag{8}$$

In the above equations f_b^- and f^- are the biaxial and uniaxial compressive strengths respectively, $\bar{I}_1$ denotes the first invariant of the effective stress tensor, $\bar{J}_2$ the second invariant of the effective deviatoric stress tensor, while $\bar{\sigma}_{max}$ and $\bar{\sigma}_{min}$ stand for the maximum and minimum principal stress respectively. The failure surface for the case of the plane stress is shown in Figure 1. $H\left[\bullet\right]$ denotes the Heaviside step function. Tensile damage is activated for stress states within the first, second and fourth quadrants of the principal stress space, see Figure 1, while compressive damage for stress states only within the third quadrant.

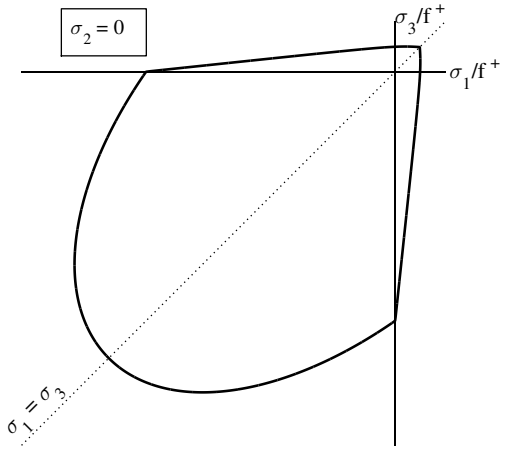

Fig. 1: Adopted damage surface under plane-stress conditions [26].

The damage criteria are defined then as [62]

$$\Phi^{\pm}\left(r^{\pm}, \tau^{\pm}\right) = \tau^{\pm} - r^{\pm} \leq 0 \tag{9}$$

where $r^{\pm}$ are internal stress-like variables that represent the current damage thresholds and the respective expansion of the damage surface. As a consequence, their initial values are equal to the uniaxial stress under tension $r_0^+ = f^+$ and compression $r_0^- = f^-$ and thereafter vary according to

$$r^{\pm} = max\left[r_0^{\pm}, \max_{i \in (0,n)} \left(\tau_i^{\pm}\right) \right] \tag{10}$$

The evolution of the internal damage variables $d^{\pm}$ is defined as [63]

$$d^{\pm} = 1 - \frac{r_0^{\pm}}{r^{\pm}} \exp\left\{ 2H_d^{\pm} \left(\frac{r_0^{\pm} - r^{\pm}}{r_0^{\pm}} \right) \right\} \tag{11}$$

In the above Equation (11), $H_d^{\pm} \geq 0$ stands for the discrete softening parameter, included to ensure mesh-size objective results considering the compressive and tensile fracture energy of the material $G_f^{\pm}$ and the characteristic finite element length. In particular, the specific dissipated energy (i.e. dissipated energy per unit of volume) in tension or compression $D^{\pm}$ is regularized considering the characteristic crack width l_{dis} related to the area (for two-dimensional elements) or volume (for three-dimensional elements) of each finite element in the crack band according to the equation [64]

$$D^{\pm} l_{dis} = G_f^{\pm} \tag{12}$$

The specific dissipated energy for a damage model with exponential softening is [65]

$$D^{\pm} = \left(1 + \frac{1}{H_d^{\pm}}\right) \frac{\left(f^{\pm}\right)^2}{2E} \tag{13}$$

From Equations (12) and (13) the previously introduced softening parameter is defined as

$$H_d^{\pm} = \frac{l_{dis}}{l_{mat} - l_{dis}} \tag{14}$$

For the current work, two-dimensional linear triangular elements are used with $l_{dis} = \sqrt{2A}$, where A denotes the area of each element. This selection can be refined according to the work of Oliver [66]. The material characteristic length l_{mat} and the discrete softening parameter H_{mat} depend only on the material properties according to [16, 65]

$$l_{mat} = \frac{1}{H_{mat}} = \frac{2EG_f^{\pm}}{\left(f^{\pm}\right)^2} \tag{15}$$

It is noted that regularized stress versus strain models, as the present one, can be shown to be equivalent to traction versus displacement jumps models such those used in fracture mechanics [67], X-FEM and E-FEM formulations [68].

3 Modelling of cracking with a local tracking technique

As discussed in the Introduction, most of the currently available crack-tracking algorithms focus on the simulation of cracks starting from the boundary of the discretized domain and propagating towards a single orientation. This drawback limits the application of such algorithms, which cannot be applied to the analysis of structures experiencing internal cracking such as shear cracks. To overcome this limitation, in this work the local-crack tracking algorithm presented by Cervera et al. [16] is adequately enhanced for the simulation of cracking initiating from internal elements of the mesh and propagating along two opposite orientations. This section presents the main features of the algorithm focusing on its novel contributions. The method is here applied to constant strain three node elements but it can be extended to other types of two-dimensional finite elements (see [17]).

The local crack-tracking algorithm constitutes an enhancement of the classical smeared crack approach. The algorithm is called at the beginning of each load increment of the numerical analysis prior to the evaluation of the stresses. Its purpose is to identify and "label" the elements pertaining to a crack path for the current increment. For these elements, the evaluation of the stresses is computed according to the nonlinear constitutive law defined in Section 2. Contrariwise, the elements falling out of the crack path will keep their linear elastic stress-strain relation.

The first procedure carried-out by the crack-tracking algorithm is the identification of new cracks. A new crack starts at an element according to the tensile damage criterion defined by Equations (5) and (9). The above check is performed throughout the whole discretized domain and not only at the elements lying over the boundary as in existing crack-tracking algorithms. This is necessary to identify and allow the initiation of internal cracking. The elements satisfying the failure criterion of Equation (9) ($\Phi^+ = 0$) are defined as *crack root* elements.

The control of the damage dispersion over a small part of the discretized domain, and thus the simulation of separate and individual cracks, is possible with the use of an *exclusion radius* criterion. This criterion, introduced in [16], defines as a crack root element the one with the highest value of the tensile equivalent stress τ^+ within a radius r_{excl} (see Figure 2a). The value of r_{excl} is defined *a priori*, and may be according to the mesoscale geometry of the heterogeneous material.

Following the above procedure, the coordinates of the *crack origin* are defined and stored. These depend on the location of the crack root element within the discretized domain. For the family of internal crack root elements, the crack origin is defined as the centroid of the triangular element, i.e. the intersecting point of the medians (Figure 2a). The same holds for corner elements, whereas for the remaining boundary elements the midpoint of the side lying on the mesh boundary is selected.

The second part of the algorithm, after the definition of the crack root and crack tip elements, is the identification of the following elements pertaining to the crack path. The procedure is different for the two crack root elements, i.e. boundary and internal ones. For each

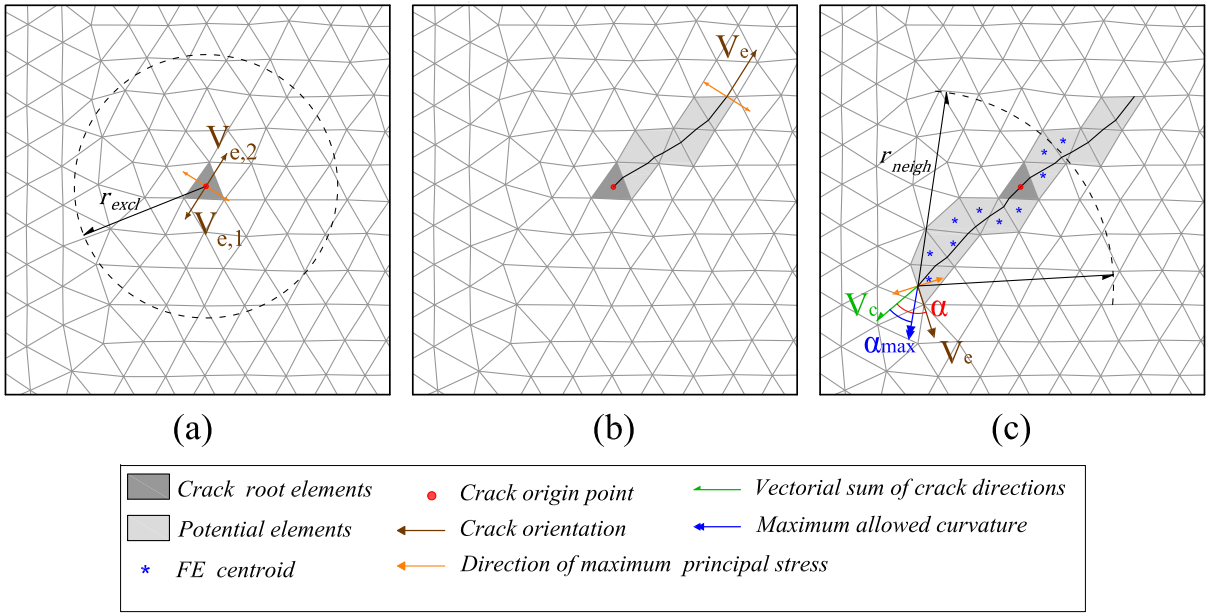

Fig. 2: Simulation of internal cracking with the crack-tracking technique: (a) *internal crack root* element with the two opposite vectors of the crack propagation, (b) labelling of the next potential elements towards the first side of the crack, (c) labelling of the next *potential* elements towards the second side of the crack and use of the *maximum curvature criterion*.

boundary crack root element, a vector is drawn, starting from the crack origin location, with a direction perpendicular to the one defined by the maximum principal stress. The intersection of this vector with the neighbouring element defines the exit point and the *next potential element* of the crack. Similarly, starting from this point the following next potential elements of the crack are recognised. The same procedure is followed for identifying the propagation path of consolidated cracks from the crack tip elements. In this case the crack origin point is the exit point of the crack at the previous cracked element.

Contrarily to cracking starting from the boundary, other cracks, such as shear ones, initiate from the interior and propagate along two opposite orientations. To account for this damage typology, the algorithm is enhanced with a different procedure. Starting from the crack origin point of the *internal crack root* element, two vectors $(\overrightarrow{V}_{e,1})$ and $(\overrightarrow{V}_{e,2})$ are defined, having a direction perpendicular to that of the maximum principal stress but opposite orientations (Figure 2a). Following this, the identification of the potential cracking elements within the current increment takes part in two steps. First, the elements pertaining to the path defined by the orientation of vector $(\overrightarrow{V}_{e,1})$ are identified starting from the crack origin point and following the same process as described above for the boundary crack root elements (Figure 2b). Upon concluding the labelling towards that side of the crack, the elements lying at the opposite face can be recognised starting again from the crack origin point of the internal crack root, but using the orientation of vector $(\overrightarrow{V}_{e,2})$ (Figure 2c). Figure 3 presents the main steps of the labelling in case of internal cracks.

The described procedure for the definition of crack propagation stops on three alternative conditions: (i) when the next potential element belongs to a different crack, i.e. when the crack joins another one (*meeting* criterion in Figure 3); (ii) when a crack reaches the mesh boundary (*boundary* criterion in Figure 3); (iii) when the stress-state of a potential element is lower than a pre-defined threshold (*stress threshold* criterion in Figure 3). This threshold can be conveniently defined in terms of the failure criterion and experience has demonstrated that labelling can be completed when the inequality $\frac{\tau^+}{f^+} < 0.75$ holds [16].

The selection of the elements of a crack depending on the local values of the stresses justifies the "local" nature of the presented crack-tracking algorithm. Even if this choice is very convenient in terms of computational efficiency and for cases of multiple cracks comparing to the global crack-tracking algorithms [16], it can meet some difficulties under bending stress states, when the local calculation of the principal stress di-

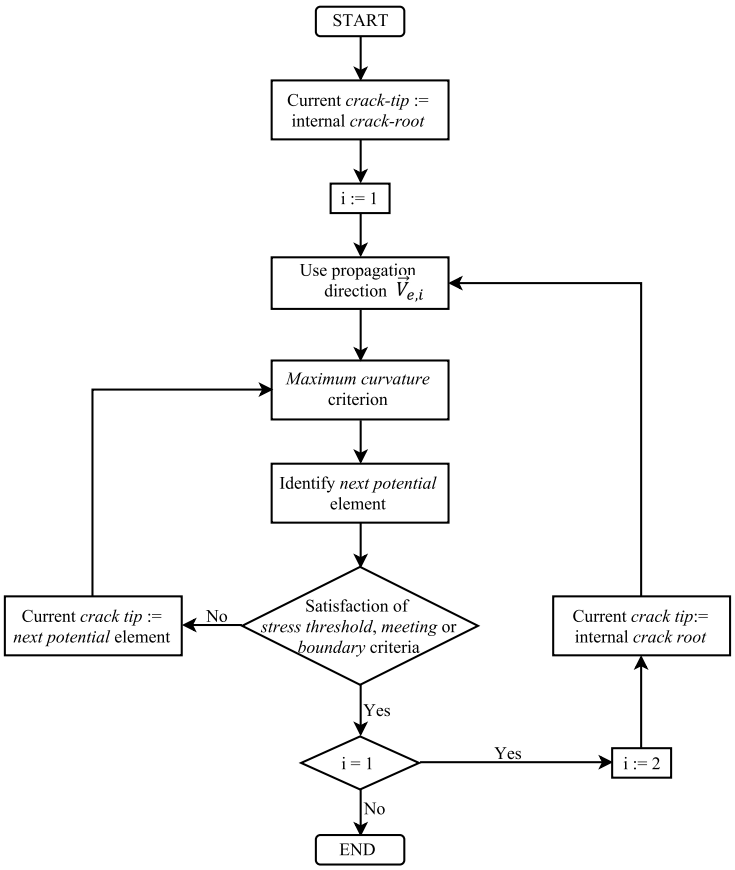

Fig. 3: Flowchart including the main steps of the crack-tracking algorithm for the identification of crack paths starting from the interior of the discretized domain.

rections may be relatively poor due to the high stress-gradients, resulting in spurious changes in the crack direction. To avoid such non-realistic result, the algorithm is enhanced with a procedure for the *apropos* correction of the crack propagation. This procedure, termed as *maximum curvature*, is activated at each element lying at the propagating front of the crack before the selection of the next potential element. The idea is to compare the crack direction defined at the element ($\overrightarrow{V_e}$), according to the principal stresses, to the direction of the vectorial sum of the crack directions ($\overrightarrow{V_c}$) of both the potential and the damaged elements within a neighbourhood of radius r_{neigh} (see Figure 2c). If the relative angle among them is larger than a maximum angle a_{max}, the vector $\overrightarrow{V_c}$ is used for the definition of the crack direction. The values of r_{neigh} and a_{max} are explicitly pre-defined.

Upon concluding the above procedure for all crack root and crack tip elements, the crack-tracking algorithm ends. The elements labelled as potential, as well as the already damaged ones, will be allowed to damage according to the constitutive model described in Section 2. For the rest, the stress-strain relationship will remain linear elastic for the current load increment.

The flexible design format of the presented algorithm can allow its possible enhancement to account for diverse problems. A branching criterion at the crack-root/tip elements would allow the simulation of crack-branching problems. However, the development of reliable criteria is necessary for a successful combination with tracking algorithms [20]. Another important extension, currently under development by the authors, concerns the modelling of intersecting cracks. This improvement can allow the simulation of problems including load-reversal (e.g. seismic actions).

4 Numerical examples

This section presents two examples to demonstrate the capacity of the proposed crack-tracking algorithm to simulate internal and multiple localized fracture in quasi-brittle materials. The first one is the Brazilian splitting

test, being a case of internal cracking propagating towards the two ends of the tested specimen. The second one is a frame wall with a door opening, tested against in-plane loading. Both examples demonstrate the capacity of the proposed technique to simulate boundary, internal and multiple localized cracks.

4.1 Benchmark for mesh objectivity: Brazilian splitting test

The first numerical application considers the simulation of the Brazilian splitting test. This example has three objectives. Firstly, to validate the capacity of the proposed algorithm to simulate cracking that initiates from the interior of the discretized domain and propagates along two opposite orientations. Secondly, to investigate the dependency of the tracking technique on the mesh discretization, both in terms of direction and size of the finite elements. Finally, to provide information regarding the computational cost induced by the use of the tracking algorithm.

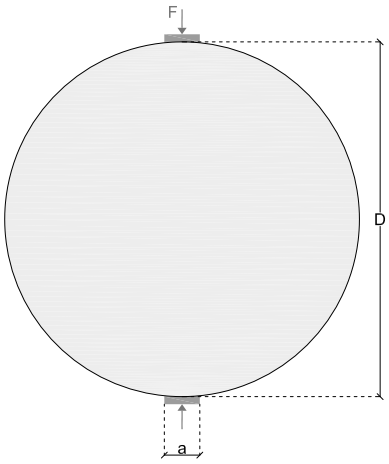

Fig. 4: Geometry and testing scheme of the Brazilian splitting test.

4.1.1 Experimental set-up and failure pattern

In the Brazilian splitting test, the tested specimen has a circular cross-section of diameter D and a depth l (Figure 4). The test consists in applying a compressive force along the diameter of the tested cylinder until failure occurs. The failure pattern is characterized by a tensile crack, starting from the interior of the tested specimen and propagating towards the boundaries following the direction of the applied compressive forces, i.e. along the diameter of the tested specimen. The obtained value of the maximum load is used to define the splitting tensile strength of the tested material. The Brazilian splitting test is a standard method for the estimation of the splitting tensile strength of geomaterials such as concrete [69] and rocks [70].

4.1.2 Numerical simulation

The dimensions considered in the numerical simulation, with respect to Figure 4, are $D = 15\ cm$, $a = D/10 = 1.5\ cm$. The cylinder is analysed under plane strain conditions. Typical material properties for concrete have been adopted: $E = 30.1\ GPa$, $f^+ = 2.2\ MPa$, $v = 0.25$, $f^- = 20\ MPa$, $= 2400\ kg/m^3$, $G^+ = 50\ J/m^2$, $G^- = 15000\ J/m^2$. The tracking parameters are r_{excl}= 0.5 cm, $a_{max} = 45°$ and r_{neigh} = 0.5 cm.

The experiment is simulated by imposing a vertical displacement at the top of the upper bearing plate. The numerical solution of the discrete problem is performed in a step-by-step manner. At each step, the corresponding nonlinear equations are solved with the use of a full Newton-Raphson method along with a line-search procedure. Convergence of an increment is attained when the ratio between the iterative residual forces and the norm of the total external forces is lower than 10^{-3} (0.1%).

The numerical calculations are performed with an enhanced version of the finite element programme COMET [71], while pre- and post-processing with GiD [72]. Both software have been developed at the International Center for Numerical Methods in Engineering (CIMNE), in Barcelona.

4.1.3 Mesh-induced bias

This section focuses on the sensitivity of the numerical solution to the typology of the used discretization, both in terms of orientation and size of the finite elements.

Figure 5 presents the four meshes used for studying the dependency of the numerical solution on the direction of the mesh. The first two are discretized in an unstructured manner with average element sizes, at the region where damage is expected, h_e=0.5 cm (984 nodes, Figure 5a) and h_e=0.25 cm (1711 nodes, Figure 5b), respectively. The same region is discretized in a structured manner in the last two meshes, with average element sizes h_e=0.5 cm. It is noted these meshes have been designed avoiding the alignment of the predominant directions of the triangular elements with the vertical axis, where the cracking is expected to occur. This has been done to show the capability of the numerical

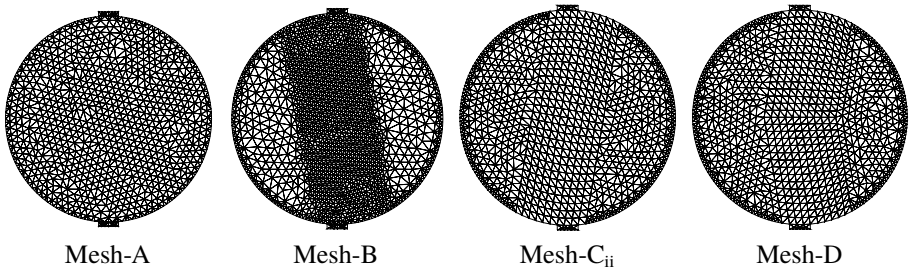

Fig. 5: The four meshes used for the mesh-induced directional bias study.

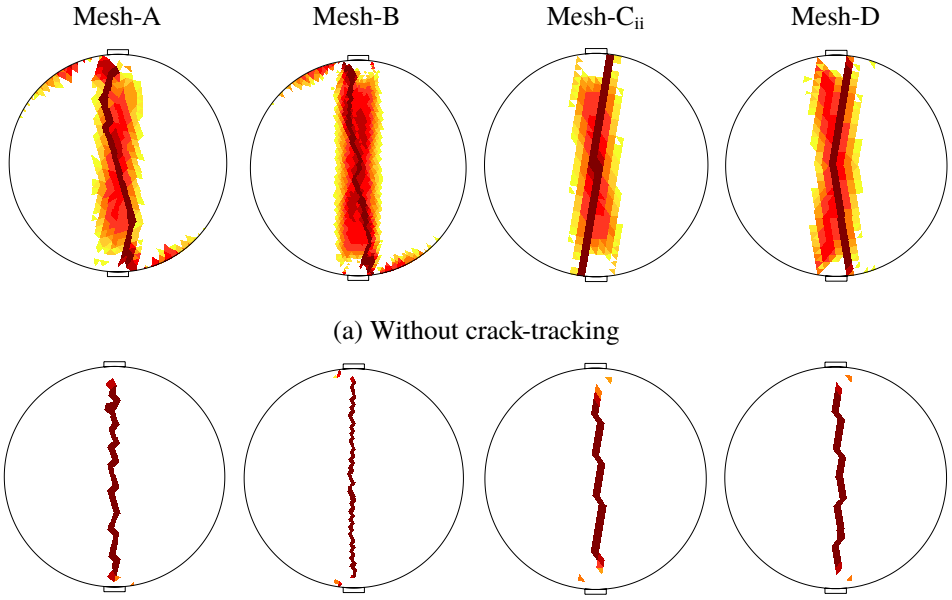

Fig. 6: Mesh-induced directional bias sensitivity. Contour of the tensile damage index (d^+) after the peak load for four different meshes: (a) without the crack-tracking algorithm, (b): with the crack-tracking algorithm.

technique to provide mesh-bias independent results. In particular, for the structured mesh Mesh-C (994 nodes, Figure 5c) the sides of the rectangular triangles create angles of around -10°, 80°, 125° with the horizontal axis. In the structured mesh Mesh-D (1016 nodes, Figure 5d) the structured region has been split into two, with the triangles in the lower part being a mirror of the ones in the upper part.

Figure 6 presents the contour of the d^+ tensile damage index for both the analyses with and without the use of the proposed tracking algorithm. The results using the classical smeared crack approach present a large spreading of damage within the discretized domain. In addition, the localization of damage depends spuriously on the mesh. This can be better visualised in the plot of the maximum principal strains, in Figure 7. The use of the tracking algorithm successfully addresses the aforementioned flaws of the classical smeared crack approach, resulting in a vertical crack emanating from the interior of the mesh and propagating along the loading direction for all the used meshes.

Apart from the sensitivity of the numerical solution on the directionality of the mesh, the effect of the finite element size is also investigated. To this aim, simulations have been performed with two additional meshes keeping the mesh-orientation of Mesh-C, but changing the sizes of the finite elements. Mesh-C' has mean element sizes h_e=0.075 m (384 nodes, Figure 8a), while in Mesh-C" h_e=0.025 m (1983 nodes, Figure 8c).

The refinement of the mesh has no positive effect on the simulation of the expected crack direction using the classical smeared crack-approach (Figures 9a and 10a).

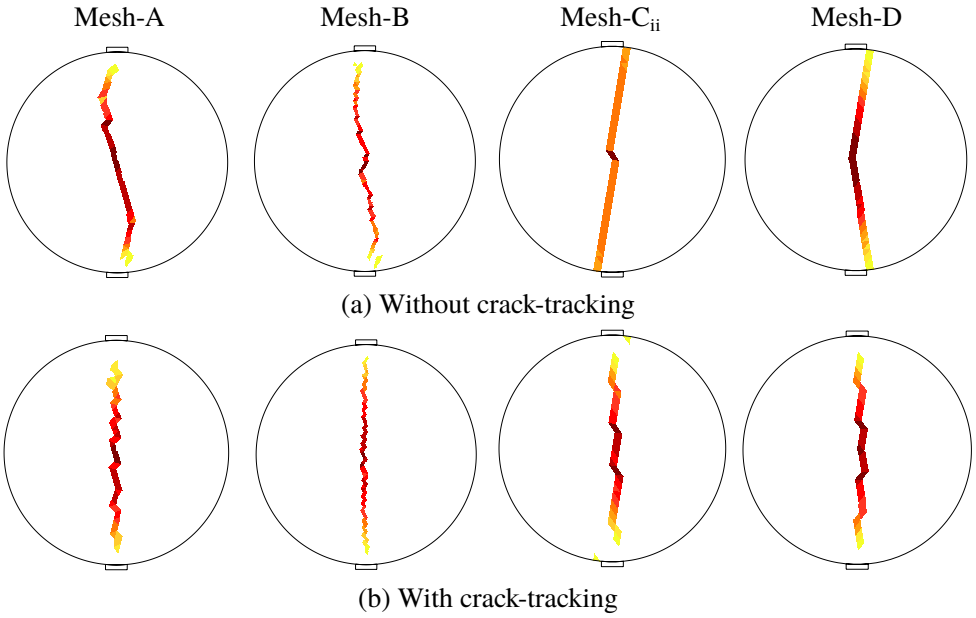

Fig. 7: Mesh-induced directional bias sensitivity. Contour of the maximum principal strains (σ_{max}) after the peak load for the four different meshes: (a) without the crack-tracking algorithm, (b): with the crack-tracking algorithm.

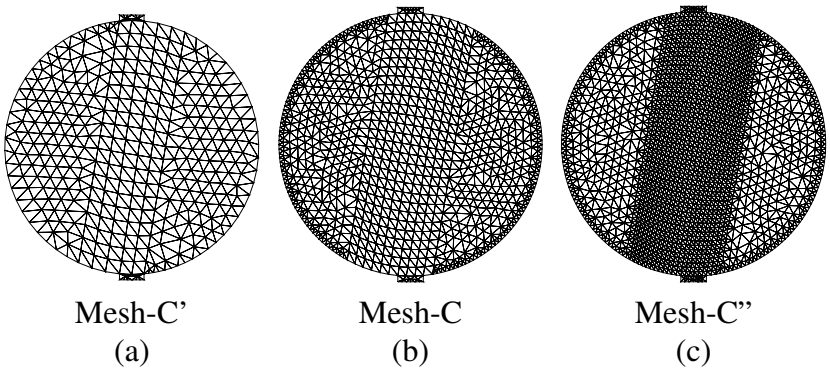

Fig. 8: The three meshes used for the mesh-size sensitivity study.

A vertical crack could not be simulated, even in the finer mesh, and the spurious spreading of damage around the localized band does not reduce on mesh refinement (Figure 9a). On the other hand, the use of the tracking algorithm predicts the expected vertical crack pattern independently of the discretization size (Figure 9b and Figure 10b.

Table 1 presents a comparison among the peak load obtained for each of the performed analysis and the analytical solution. The latter is calculated through the formula proposed by [69, 70] that is

$$P/l = \frac{\pi D f_{sp}}{2} \tag{16}$$

where P/l is the capacity per unit length and f_{sp} is the splitting tensile strength. Its value is considered equal to $f_{sp} = f^{+}/0.9$ according to Eurocode 2 [73]. Good agreement with the analytical result is achieved when the tracking algorithm is used. Contrariwise, the large spreading of damage in the numerical solution without the tracking algorithm lowers unrealistically the capacity of the specimen.

4.1.4 Computational cost

Table 2 presents the computational cost, in terms of time and memory resources, needed for the performed analyses with and without the tracking-algorithm. All the numerical analyses have been performed in a single machine equipped with an Intel Core i7-4790-3.60GHz CPU and 16.0 GB RAM.

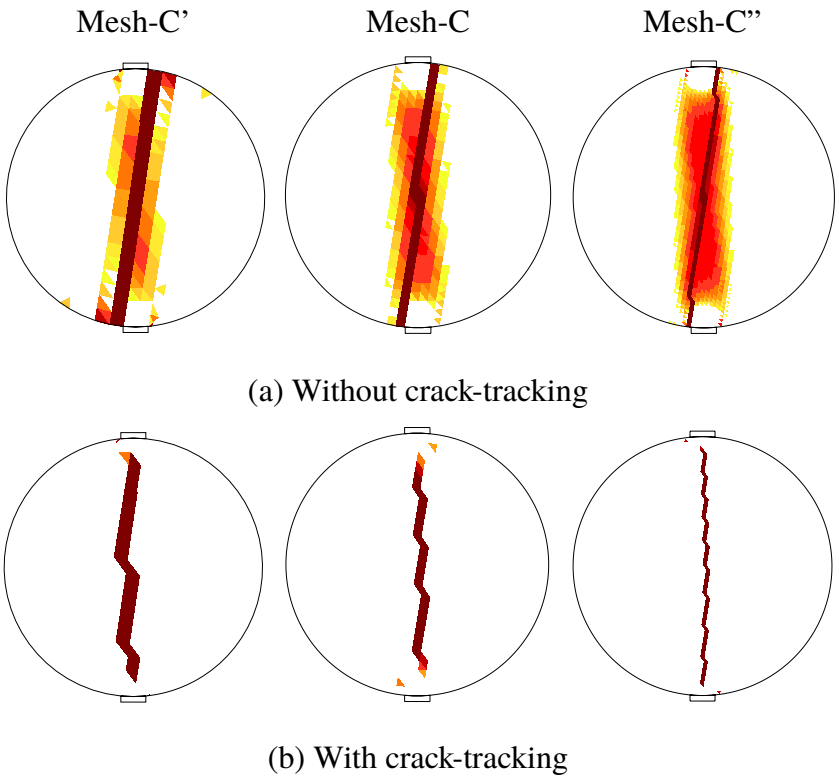

Fig. 9: Mesh-size sensitivity. Contour of the tensile damage index (d^+) after the peak load for four different meshes: (a) without the crack-tracking algorithm, (b): with the crack-tracking algorithm.

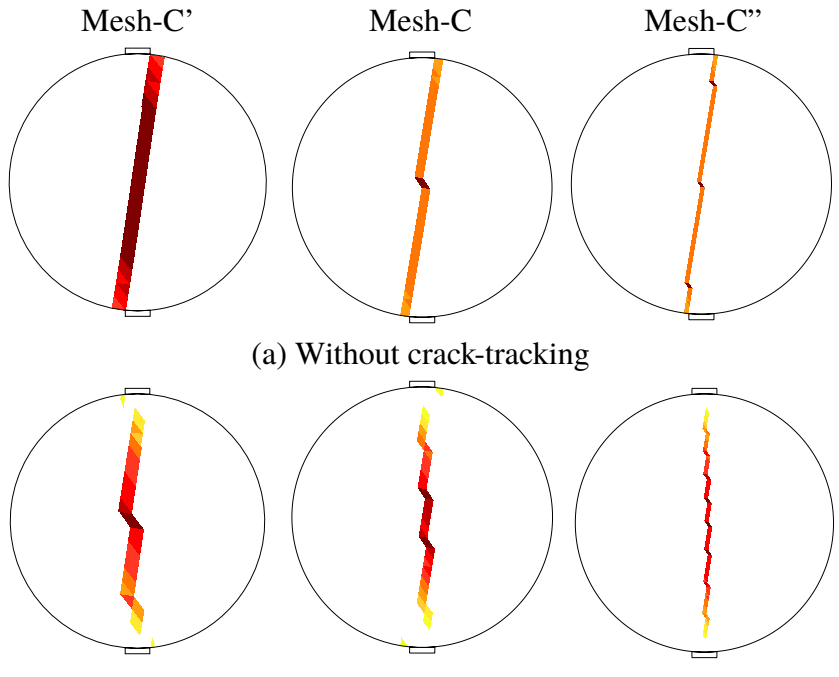

Fig. 10: Mesh-size sensitivity. Contour of the maximum principal strains (σ_{max}) after the peak load for the four different meshes: (a) without the crack-tracking algorithm, (b): with the crack-tracking algorithm.

		No-Tracking		Tracking	
Mesh	Analytical capacity $[kN/m]$	Capacity $[kN/m]$	Difference from analytical [%]	Capacity $[kN/m]$	Difference from analytical [%]
Mesh-A	575.96	537.56	-6.67	579.39	0.60
Mesh-B	—"—	538.22	-6.55	585.29	1.62
Mesh-C'	—"—	514.98	-10.06	539.65	-6.30
Mesh-C	—"—	529.66	-8.04	544.44	-5.47
Mesh-C"	—"—	532.35	-7.57	549.10	-4.66
Mesh-D	—"—	529.14	-8.13	554.09	-3.80

Table 1: Comparison between numerical and analytical results with and without the proposed tracking algorithm for the Brazilian splitting test.

		No-Tracking		Tracking		Overhead using tracking	
Mesh	Number of nodes	Memory [Mb]	CPU-time [s]	Memory [Mb]	CPU-time [s]	Memory [%]	CPU-time [%]
Mesh-A	984	1.33	14.52	1.56	13.06	17.29	-10.06
Mesh-B	1711	2.37	28.66	2.78	24.96	17.30	-12.91
Mesh-C'	384	0.52	4.38	0.61	5.07	17.31	15.75
Mesh-C	994	1.35	10.47	1.58	13.15	17.04	25.60
Mesh-C"	1983	2.76	24.98	3.24	32.74	17.39	31.06
Mesh-D	1016	1.38	10.61	1.62	13.48	17.39	27.05

Table 2: Computational cost with and without the use of the tracking algorithm for the Brazilian splitting test.

As can be seen, the tracking algorithm is very efficient both in terms of memory requirements and computational time. The arrays necessary for the labelling system of the elements result to additional memory requirements of around 17 % using the tracking algorithm. The performed analyses show that the computational time overhead using tracking increases, as expected, with the increase of the number of degrees of freedom, with a maximum overhead of around 31% for the case of the refined Mesh-C". Note that in some cases (Mesh-A and Mesh-B) the computational cost using the tracking algorithm is lower than a calculation done without using it. This is because of the improvement of the non-linear iterations convergence rate due to the correct damage localization when using the tracking algorithm.

4.2 Structural Application: Frame wall with one door opening

In this section, we investigate the capacity of the proposed algorithm to simulate the response of a large-scale structural problem exhibiting multiple cracking. The simulated experiment consists in the in-plane lateral loading of a full-scale unreinforced masonry frame with an opening [74]. This structural example has been selected due to the complexity given by the structural interaction among the piers and the spandrel, representing a meaningful case with different types of cracks due to traction, shear and flexure. In fact, this test can show the capacity of the used approach to represent both the experimental cracking pattern and the redistribution of actions among structural members as soon as the different cracks appear.

4.2.1 Experimental setting and results

The masonry is built of yellow tuff bricks with dimensions 150 × 300 × 100 mm^3 and hydraulic mortar of 100 mm thickness. The wall has overall dimensions of 5100 mm length, 3620 mm height and 310 mm thickness. The spandrel above the opening lies over a timber lintel with bond length of 150 mm at both sides.

The experimental test was performed in two steps. Initially, a distributed load was applied at the top of each pier with a resultant $V = 200\ kN$. This was followed by the application of a horizontal displacement d at the left of the wall keeping the vertical load constant. Figure 11a illustrates the geometry and the load configuration of the experiment. Figure 11b and Figure 11c show the resulted cracking in the whole structure and the spandrel respectively. The in-plane loading activated different failure phenomena in masonry resulting in a complex cracking of the structure. In particular, two horizontal cracks formed at the base of the piers due to the debonding between the units and the mortar. Flexural cracking, crossing both the units and

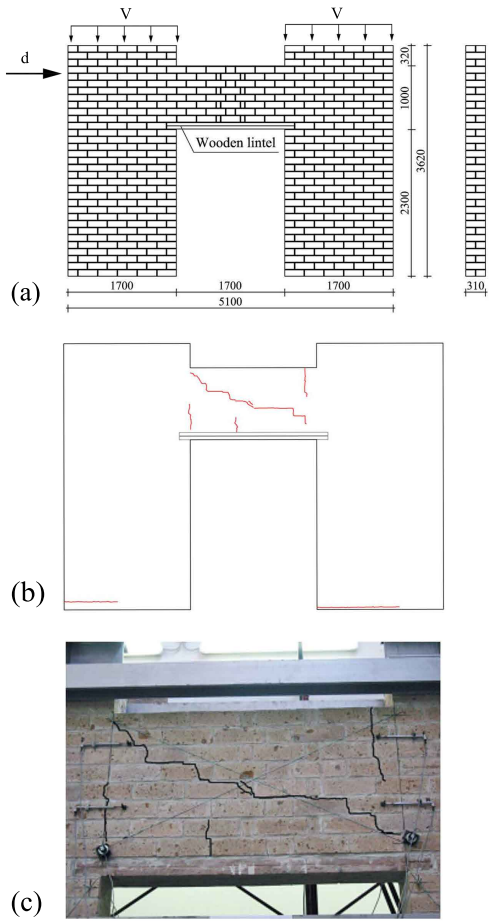

Fig. 11: (a) Geometry and load configuration of the experiment. Cracking after the end of the experiment of (b) the whole frame and (c) the spandrel (pictures adapted from [74].

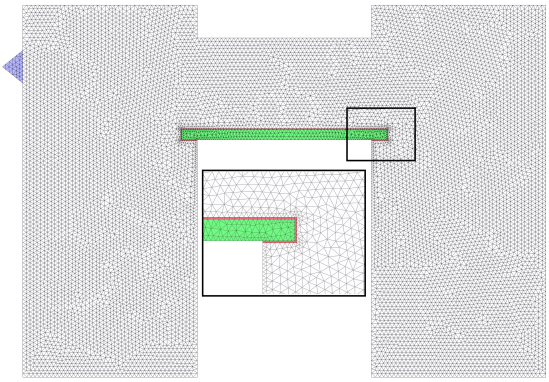

Fig. 12: Discretized domain used for the numerical simulation.

mortar-units interface, appeared in three locations at the lower and the upper part of the spandrel. Finally, the last reported damage was a diagonal shear crack starting from the middle of the spandrel and extending diagonally towards its opposite corners. For a detailed description of the experimental setup, the loading procedure and the damage pattern the reader is referred to the original work [74].

4.2.2 Numerical simulation

The experimental test is simulated using the numerical algorithm presented in Section 3. The material of the wall is idealized as homogeneous with its properties derived from the available experimental data [74], while appropriate values from the literature are chosen for the non-available material parameters. The constitutive model of Section 2 is used as an approximation of the masonry behaviour. In this work, focus is given on the capacity of the algorithm to simulate the different typologies of the localized cracking observed in the particular example.

For masonry, the selected material properties are $E = 1.54\ GPa$, $f^+ = 0.13\ MPa$, $v = 0.2$, $f^- = 3.9\ MPa$, $= 1200\ kg/m^3$, $G^+ = 15\ J/m^2$, $G^- = 35000\ J/m^2$, while the ratio between uniaxial and biaxial compressive strength is considered as $f_b^-/f^- = 1.15$. Linear elastic behaviour is assumed for the timber lintel with Young's modulus $E = 15\ GPa$. The connection between the masonry and the timber lintel is modelled with care in order to provide a realistic representation of the actual interaction between the two neighbouring materials. This interconnection is modelled through a soft layer with thickness of 10 mm and limited strength and stiffness ($E = 0.02\ GPa$, $f^+ = 0.01\ MPa$, $v = 0.2$, $f^- = 3.9\ MPa$, $G^+ = 5\ J/m^2$, $G^- = 35000\ J/m^2$). This zone can be seen as the continuous counterpart of a no-tension discontinuous interface.

Following the experiment, the numerical simulation consists of two steps: first, the application of the dead load along with a vertical force equal to 200 kN at the top of each pier, and second, the incremental application of a horizontal displacement at the left part of the structure, keeping the load of the first step constant.

The masonry frame is discretized in an unstructured mesh of 2D plane-stress three-noded triangles with average mesh size of $h_e = 4\ cm$ (10678 nodes) (Figure 12). In the reference case the input parameters for the local crack-tracking algorithm are r_{excl}= 300 mm (equal to the length of the bricks), $a_{max} = 45°$ and r_{neigh} = 200 mm. The influence of these values is investigated in Section 4.2.5.

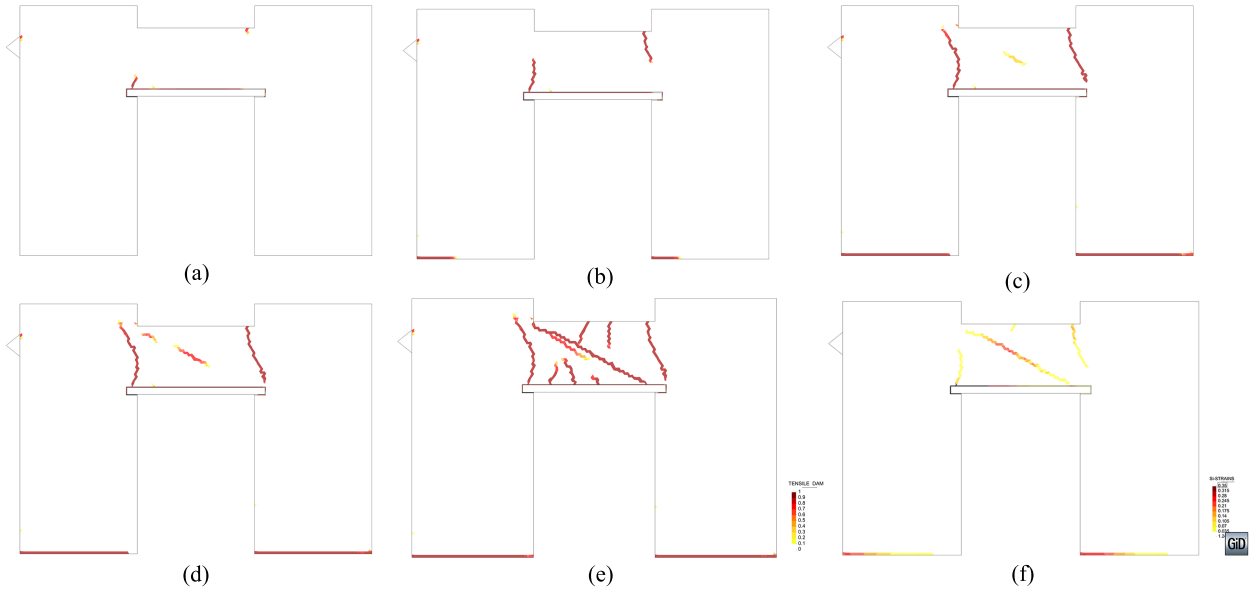

Fig. 13: Tensile damage contour for: (a) $d = 1.5\ mm$, (b) $d = 3.3\ mm$, (c) $d = 12.3\ mm$, (d) $d = 17.3\ mm$, (e) $d = 20.7\ mm$. (f) Maximum principal strains contour for $d = 20.7\ mm$.

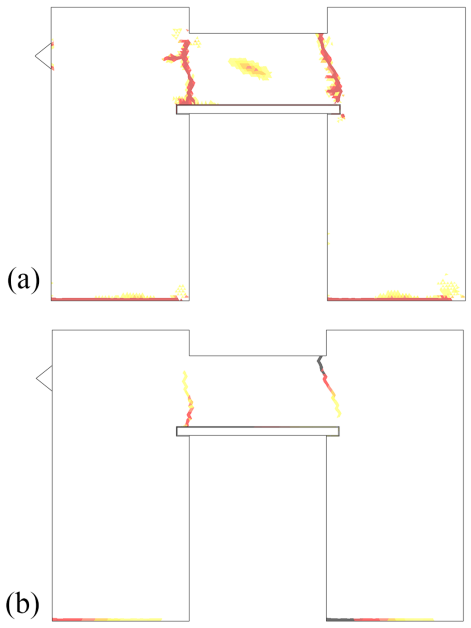

Fig. 14: Tensile damage contour (a) and maximum principal strains (b) for the analysis with the smeared crack approach without a crack-tracking technique (horizontal displacement $d = 25\ mm$)

4.2.3 Results and discussion

Figure 13 illustrates the sequence of the tensile cracks obtained from the numerical analysis. In the first part of the numerical simulation, which includes the application of the dead load as well as the load of 200 kN at the top of the piers, no damage occurs. Two vertical cracks at the corners of the spandrel are the first damage occurring in the structure during the second stage of the analysis (Figure 13a). An increase of the horizontal displacement results in the formation of two horizontal cracks at the base of the piers (Figure 13b) and their subsequent rocking. Following this, internal cracking starts to form within the spandrel (Figure 13c-d). Finally, at a horizontal displacement of 21 mm, a diagonal shear crack has totally formed and secondary flexure cracks are observed at the top and bottom of the spandrel (Figure 13e).

It can be appreciated in Figure 13f that the obtained damage is in good agreement with the resulted cracking pattern of the experiment (Figures 11b-c). The open localized cracks at the end of the analysis, displayed by the contour of the tensile principal strains in Figure 13f, are located at the both ends of the spandrel, at its middle and at the bottom of the piers as in the experiment.

Finally, it is noted that the numerical simulation of this particular example would be impossible using a crack-tracking technique without the enhancement for internal cracking. Apart from the internal shear cracking affecting the middle of the spandrel, the flexural cracks at its left bottom do not start from the boundary of the numerical domain.

The numerical result using the classical smeared crack approach, without the enhancement given by a crack-tracking technique, is illustrated in Figure 14.

Cracking at the base of the piers is almost localized within a single row of elements, facilitated by the alignment of the mesh with the expected crack direction. Contrarily, a dispersion of the damage can be observed at the region of the flexural cracks at the spandrel, where the solution is biased by the mesh topology. This spurious spreading of the damage results in the unrealistic release of elastic energy due to the elastic unloading of the elements surrounding the damaged ones. As a consequence, the capacity of the structure reduces before reaching the necessary force for the opening of the internal shear crack that was observed experimentally. This limitation of the classical smeared crack approach prevents to capture correctly the experimental obtained damage.

Figure 15 presents the smeared cracking strain field resulting from a numerical analysis of the same experiment performed with a micro-model approach by Parisi et al. [75]. The results obtained with the tracking algorithm (see Figure 13e & Figure 13f) agree with the damage pattern simulated by the micro-model.

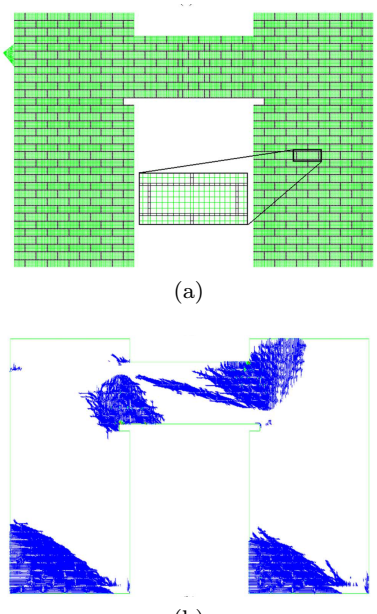

(a)

(b)

Fig. 15: Micro-model used in [75] for the simulation of the in-plane loaded masonry frame: (a) mesh, (b) smeared cracking strain field (pictures adapted from [75]).

Figure 16 presents the comparison between the numerical and experimental load-displacement diagrams. The use of the crack-tracking algorithm allows to capture correctly the experimentally obtained failure curve, both in terms of maximum strength and ductility of the

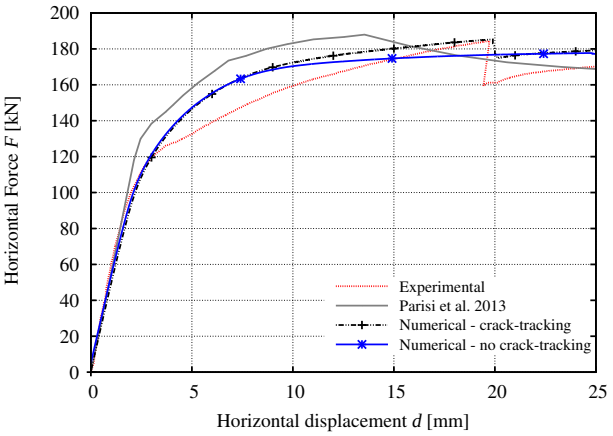

Fig. 16: Load-displacement graph of the experimental test and the numerical analyses.

structure. The first significant loss of stiffness is related to the rocking of the piers and the relative cracking at their base, which results in the increasing opening of the flexural cracks at the two opposite ends of the spandrel (see Figure 13b). The latter damage is the dominating cause for the loss of stiffness of the structure until the shear crack forms in the spandrel, which results in the sudden drop of the applied force for a displacement of about 20 mm.

An important aspect of the numerical result is its capacity to reproduce satisfactorily the loss of structural stiffness occurring due to all the different fracture phenomena throughout the loading history. This is essential for the evaluation of the seismic capacity of an existing structure, or the design of a new one, since common procedures (e.g. [76, 77]) rely on the realistic estimation of the initial stiffness, the ductility and the strength reduction. When the crack-tracking technique is not used, the load versus displacement graph fails to represent the correct sequence of fracture in the nonlinear range, as the brittle shear cracking in the spandrel.

4.2.4 Computational cost

As in the example of the Brazilian splitting test, Table 3 presents information regarding the computational cost with and without the use of the tracking algorithm for the particular example. The additional requirements in memory lie within the same range of values as in the Brazilian splitting test, i.e around 16% higher using the tracking algorithm. The processing time with the proposed technique is around 11% higher than that of the classical smeared crack approach.

No-Tracking		Tracking		Overhead using tracking	
Memory [Mb]	CPU-time [s]	Memory [Mb]	CPU-time [s]	Memory [%]	CPU-time [%]
16.97	238.06	19.62	264.03	15.61	10.90

Table 3: Computational cost with and without the use of the tracking algorithm for the frame wall with a door opening example.

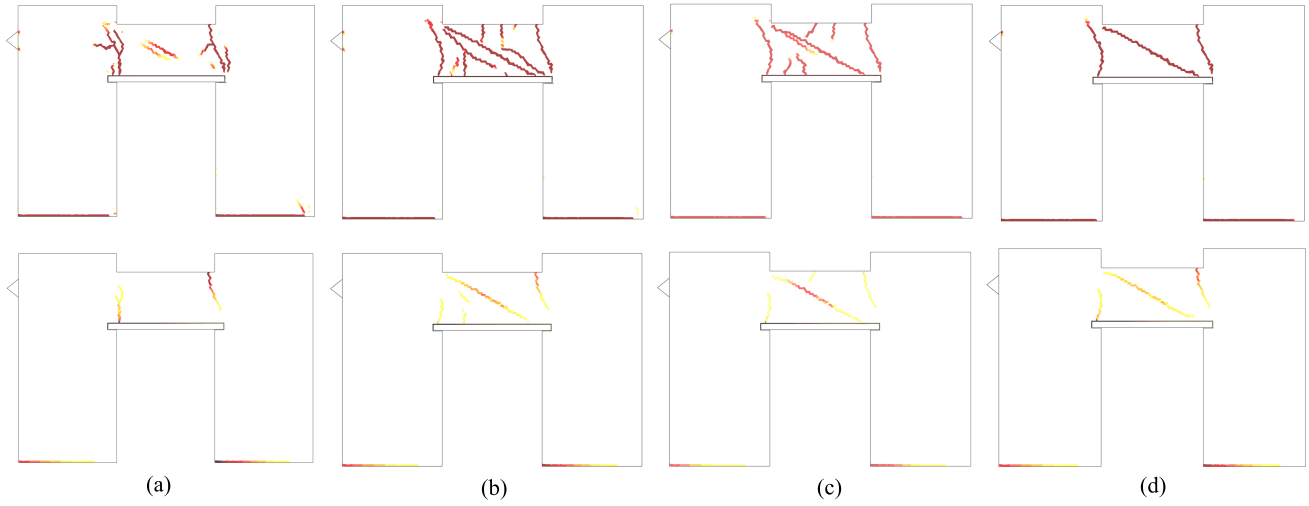

Fig. 17: Contour of tensile damage (left) and maximum principal strain (right): (a) $r_{excl} = 0.1\ m$, (b) $r_{excl} = 0.2\ m$, (c) $r_{excl} = 0.3\ m$, (d) $r_{excl} = 0.5\ m$ (horizontal displacement $d = 0.21\ m$).

4.2.5 Effect of tracking parameters

This section presents a sensitivity analysis on the crack-tracking parameters to assess their influence on the numerical results. Figure 17 presents the obtained damage pattern with four different values of the exclusion radius r_{excl}= [0.1; 0.2; 0.3; 0.5 m]. As expected, the exclusion radius r_{excl} has significant effect in the numerical simulation, affecting the distribution of cracking within the analysed structure. Values lower than the unit size result in a denser cracking within the spandrel, changing the response of the structure and the damage pattern. In particular, for $r_{excl} = 0.1\ m$ various cracks appear at the both ends of the spandrel, facilitating the rocking mode of the whole structure, while the shear crack at the middle of the spandrel cannot be reproduced. This change in the structural response can be appreciated in the load vs displacement graphs of Figure 18, where for $r_{excl} = 0.1\ m$ the typical graph for a rocking failure mode is obtained, without however, the sudden drop attributed to the shear cracking of the spandrel. On the contrary, when values higher of 0.2 m are chosen, the numerical model reproduces the experimental obtained structural response (Figure 17b-d and Figure 18). Actually, a value of the exclusion radius lower than 0.2 m does not take into account the internal microstructure of masonry defined by the size of the brick.

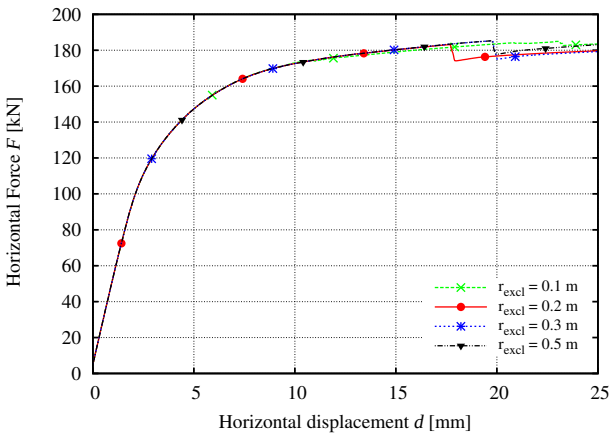

Fig. 18: Sensitivity of structural capacity to r_{excl}.

The above results demonstrate the utility of the exclusion radius. The failure mechanism of masonry structures is determined by the relative position of the cracks and consequently the division of the whole structure into macroblocks. The relative geometry and strength of the components play a decisive role in the type of cracking of masonry structures. This can be appreciated

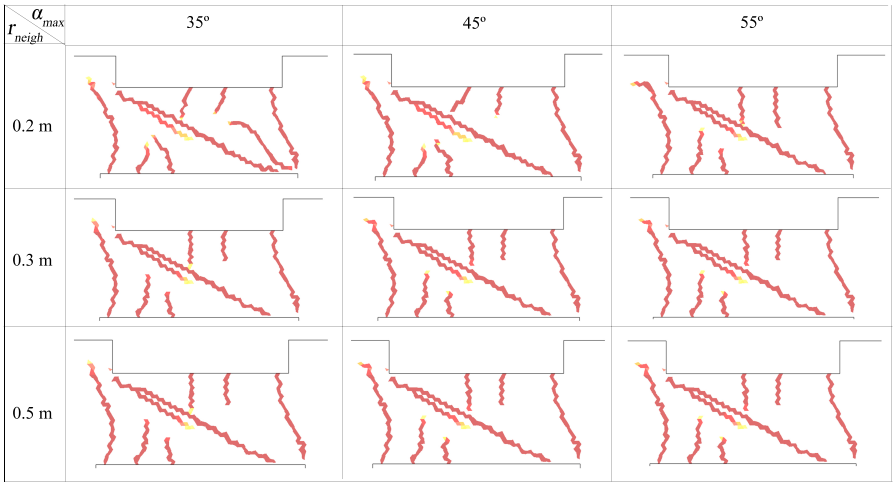

Fig. 19: Sensitivity of damage distribution at the spandrel to a_{max} and r_{neigh}.

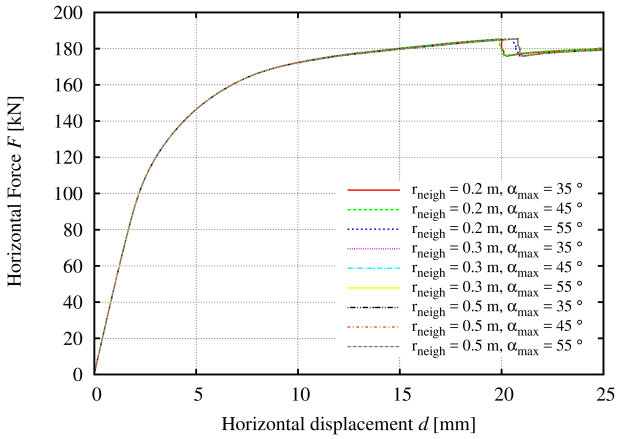

Fig. 20: Sensitivity of structural capacity to a_{max} and r_{neigh}

in the experimental test under investigation, in which cracking occurred mainly at the joints between bricks and mortar. A continuum finite element model ignores the internal geometry of the composite and therefore fails to capture failure mechanisms determined by it. This drawback can be partially overcome with the use of the exclusion radius, which can be perceived as a way to take into account the size effect of the units within a continuum finite element model. On the contrary, a micro-model could simulate this cracking phenomenon in a more direct way due to the *a priori* detailed geometrical definition of the problem, at the cost of a computation time largely higher than that of the proposed model. This disadvantage of micro-models renders them hardly applicable to the analysis of large and complex structures. The proposed model based on a crack-tracking method shows to be a good compromise between accuracy and computational cost.

Figures 19 and 20 present the cracking affecting the spandrel and the relative load against displacement curves respectively for nine different combinations of a_{max} and r_{neigh} for $r_{excl} = 0.3\ m$. Once the exclusion radius is well defined, the effect of a_{max} and r_{neigh} is minor to the global response of the structure. The shear cracking at the middle of the spandrel is identical for all combinations of the above correction parameters. This is to be anticipated, since shear cracking, dominant in this case, is not affected by these parameters, on contrary with cracking under bending stress states (see [16]). Restricting the change in the crack curvature with low values of a_{max} has a small effect on the secondary flexural cracking affecting the lower and upper boundaries of the spandrel. In any case, the collapse mechanism is identical for all the investigated values of a_{max} and r_{neigh}.

5 Conclusions

The structural behaviour of constructions made of quasi-brittle materials, such as concrete or masonry, is determined by the formation of discrete cracks that define the collapse mechanism. Continuum finite element approaches based on the classical smeared crack approach simulate poorly this complex response since (a) they may represent damage spread in an unrealistic way and (b) the numerical solution is determined by the mesh-induced directional bias.

To circumvent the above drawbacks, this article proposes the use of a crack-tracking technique for the realistic simulation of cracking in structures made of quasi-

brittle materials. A novel algorithm is presented for the simulation of cracking starting at any location within the discretized domain making possible the simulation of both boundary and internal cracking. This contribution, along with the capacity of the approach to allow the nucleation of new cracks without the *a priori* definition by the user, extends the application field of tracking algorithms to the structural assessment of new or existing structures.

Two numerical examples are used to validate the proposed algorithm: a Brazilian splitting test and the in-plane loading of a frame wall with a door opening. The numerical simulations prove the capability of the model to represent correctly the formation and propagation of tensile, flexural and shear cracks within the discretized domain. The accurate representation by the model of the cracking phenomena produces a realistic simulation of the experimental failure mechanisms and the correct estimation of the nonlinear response of the structure. The model yields a damage pattern more realistic than the well-known smeared crack approach.

The limited computational cost of the proposed approach and its accuracy render it a reliable tool for the analysis of complex structural problems experiencing multiple cracking. The tracking technique proposed for the modelling of internal cracking has shown to be robust and it can be used in conjunction with other finite element formulations and material models.

Acknowledgements This research has received the financial support from the MINECO (Ministerio de Economia y Competitividad of the Spanish Government) and the ERDF (European Regional Development Fund) through the the MULTIMAS project (Multiscale techniques for the experimental and numerical analysis of the reliability of masonry structures, ref. num. BIA2015-63882-P) and the EACY project (Enhanced accuracy computational and experimental framework for strain localization and failure mechanisms, ref. MAT 2013-48624-C2-1-P).

The authors gratefully acknowledge Dr. Fulvio Parisi for providing information regarding the experimental data.

References

1. D. Ngo and C. Scordelis, "Finite Element Analysis of Reinforced Concrete Beams," *ACI Journal*, vol. 64, no. 3, pp. 152–163, 1967.
2. Y. Rashid, "Ultimate strength analysis of prestressed concrete pressure vessels," *Nuclear Engineering and Design*, vol. 7, pp. 334–344, apr 1968.
3. J. Mosler and G. Meschke, "Embedded crack vs. smeared crack models: a comparison of elementwise discontinuous crack path approaches with emphasis on mesh bias," *Computer Methods in Applied Mechanics and Engineering*, vol. 193, no. 30-32, pp. 3351–3375, 2004.
4. R. H. J. Peerlings, R. De Borst, W. A. M. Brekelmans, and J. H. P. De Vree, "Gradient enhanced damage for quasi-brittle materials," *International Journal for Numerical Methods in Engineering*, vol. 39, no. 19, pp. 3391–3403, 1996.
5. A. Simone, G. N. Wells, and L. J. Sluys, "From continuous to discontinuous failure in a gradient-enhanced continuum damage model," *Computer Methods in Applied Mechanics and Engineering*, vol. 192, pp. 4581–4607, oct 2003.
6. Z. P. Bažant and F. B. Lin, "Nonlocal Smeared Cracking Model for Concrete Fracture," *Journal of Structural Engineering*, vol. 114, pp. 2493–2510, nov 1988.
7. J. de Vree, W. Brekelmans, and M. van Gils, "Comparison of nonlocal approaches in continuum damage mechanics," *Computers & Structures*, vol. 55, pp. 581–588, may 1995.
8. R. De Borst, "Simulation of strain localization: a reppraisal of the cosserat continuum," *Engineering Computations*, vol. 8, pp. 317–332, apr 1991.
9. R. De Borst, L. Sluys, H.-B. Mühlhaus, and J. Pamin, "Fundamental issues in Finite Element Analyses of localization of deformation," *Engineering Computations*, vol. 10, no. 2, pp. 99–121, 1993.
10. L. Benedetti, M. Cervera, and M. Chiumenti, "Stress-accurate Mixed FEM for soil failure under shallow foundations involving strain localization in plasticity," *Computers and Geotechnics*, vol. 64, pp. 32–47, mar 2015.
11. M. Jirásek and T. Zimmermann, "Embedded crack model. Part II. Combination with smeared cracks," *International Journal for Numerical Methods in Engineering*, vol. 50, no. 6, pp. 1291–1305, 2001.
12. G. N. Wells and L. J. Sluys, "A new method for modelling cohesive cracks using finite elements," *International Journal for Numerical Methods in Engineering*, vol. 50, no. 12, pp. 2667–2682, 2001.
13. N. Moës and T. Belytschko, "Extended finite element method for cohesive crack growth," *Engineering Fracture Mechanics*, vol. 69, pp. 813–833, may 2002.
14. P. Dumstorff and G. Meschke, "Crack propagation criteria in the framework of X-FEM-based structural analyses," *International Journal for Numerical and Analytical Methods in Geomechanics*, vol. 31, pp. 239–259, feb 2007.
15. M. Cervera and M. Chiumenti, "Mesh objective tensile cracking via a local continuum damage model and a crack tracking technique," *Computer Methods in Applied Mechanics and Engineering*,

vol. 196, no. 1-3, pp. 304–320, 2006.
16. M. Cervera, L. Pelà, R. Clemente, and P. Roca, "A crack-tracking technique for localized damage in quasi-brittle materials," *Engineering Fracture Mechanics*, vol. 77, no. 13, pp. 2431–2450, 2010.
17. A. Slobbe, M. Hendriks, and J. Rots, "Smoothing the propagation of smeared cracks," *Engineering Fracture Mechanics*, vol. 132, pp. 147–168, dec 2014.
18. M. Jirásek and P. Grassl, "Evaluation of directional mesh bias in concrete fracture simulations using continuum damage models," *Engineering Fracture Mechanics*, vol. 75, no. 8, pp. 1921–1943, 2008.
19. R. De Borst, "Fracture in quasi-brittle materials: A review of continuum damage-based approaches," *Engineering Fracture Mechanics*, vol. 69, pp. 95–112, 2001.
20. T. Rabczuk, "Computational Methods for Fracture in Brittle and Quasi-Brittle Solids : State-of-the-art Review and Future Perspectives," *ISRN Applied Mathematics*, vol. 2013, pp. 1–61, 2012.
21. W.-F. Chen, *Plasticity in reinforced concrete*. McGraw-Hill, 1982.
22. W.-F. Chen, *Constitutive Equations for Engineering Materials, Vol. 2 plasticity and modelling*. Elsevier, 1994.
23. P. H. Feenstra and R. De Borst, "A composite plasticity model for concrete," *International Journal of Solids and Structures*, vol. 33, pp. 707–730, feb 1996.
24. J. Mazars and G. Pijaudier-Cabot, "Continuum damage theory - application to concrete," *Journal of Engineering Mechanics*, vol. 115, no. 2, pp. 345–365, 1989.
25. M. Cervera, J. Oliver, and R. Faria, "Seismic evaluation of concrete dams via continuum damage models," *Earthquake Engineering & Structural Dynamics*, vol. 24, no. 9, pp. 1225–1245, 1995.
26. J. Lubliner, J. Oliver, S. Oller, and E. Oñate, "A plastic-damage model for concrete," *International Journal of Solids and Structures*, vol. 25, no. 3, pp. 299–326, 1989.
27. G. Lee and G. L. Fenves, "Plastic-Damage Model for Cyclic Loading of Concrete Structures," *Journal of Engineering Mechanics*, vol. 124, no. 8, pp. 892–900, 1998.
28. J. Y. Wu, J. Li, and R. Faria, "An energy release rate-based plastic-damage model for concrete," *International Journal of Solids and Structures*, vol. 43, no. 3-4, pp. 583–612, 2006.
29. E. Papa, "A unilateral damage model for masonry based on a homogenisation procedure," *Mechanics of Cohesive-Frictional Materias*, vol. 1, no. February, pp. 349–366, 1996.
30. P. B. Lourenço, "Anisotropic Softening Model for Masonry Plates and Shells," *Journal of Structural Engineering*, vol. 126, no. 9, pp. 1008–1016, 2000.
31. L. Pelà, M. Cervera, and P. Roca, "An orthotropic damage model for the analysis of masonry structures," *Construction and Building Materials*, vol. 41, pp. 957–967, 2013.
32. J. Lopez, S. Oller, E. Oñate, and J. Lubliner, "A homogeneous constitutive model for masonry," *International Journal for Numerical Methods in Engineering*, vol. 46, no. 10, pp. 1651–1671, 1999.
33. V. Kouznetsova, M. G. D. Geers, and W. A. M. Brekelmans, "Multi-scale constitutive modelling of heterogeneous materials with a gradient-enhanced computational homogenization scheme," *International Journal for Numerical Methods in Engineering*, vol. 54, pp. 1235–1260, jul 2002.
34. A. Zucchini and P. B. Lourenço, "A micro-mechanical model for the homogenisation of masonry," *International Journal of Solids and Structures*, vol. 39, pp. 3233–3255, jun 2002.
35. P. B. Lourenço, G. Milani, A. Tralli, and A. Zucchini, "Analysis of masonry structures: review of and recent trends in homogenization techniques.," *Canadian Journal of Civil Engineering*, vol. 34, no. 11, pp. 1443–1457, 2007.
36. C. Calderini and S. Lagomarsino, "Continuum Model for In-Plane Anisotropic Inelastic Behavior of Masonry," *Journal of Structural Engineering*, vol. 134, no. 2, pp. 209–220, 2008.
37. J. Oliver, M. Caicedo, E. Roubin, A. Huespe, and J. Hernández, "Continuum approach to computational multiscale modeling of propagating fracture," *Computer Methods in Applied Mechanics and Engineering*, vol. 294, pp. 384–427, 2015.
38. M. Petracca, L. Pelà, R. Rossi, S. Oller, G. Camata, and E. Spacone, "Regularization of first order computational homogenization for multiscale analysis of masonry structures," *Computational Mechanics*, dec 2015.
39. P. B. Lourenço and J. G. Rots, "Multisurface Interface Model for Analysis of Masonry Structures," *Journal of Engineering Mechanics*, vol. 123, no. 7, pp. 660–668, 1997.
40. L. Macorini and B. A. Izzuddin, "A non-linear interface element for 3D mesoscale analysis of brick-masonry structures," *International Journal for Numerical Methods in Engineering*, vol. 85, pp. 1584–1608, mar 2011.
41. S. Oliveira and R. Faria, "Numerical simulation of collapse scenarios in reduced scale tests of arch dams," *Engineering Structures*, vol. 28, no. 10,

pp. 1430–1439, 2006.
42. P. Roca, M. Cervera, G. Gariup, and L. Pelà, "Structural Analysis of Masonry Historical Constructions. Classical and Advanced Approaches," *Archives of Computational Methods in Engineering*, vol. 17, pp. 299–325, jul 2010.
43. J. Carvalho, J. Ortega, P. B. Lourenço, L. F. Ramos, and H. Roman, "Safety analysis of modern heritage masonry buildings: Box-buildings in Recife, Brazil," *Engineering Structures*, vol. 80, pp. 222–240, 2014.
44. N. Mendes and P. B. Lourenço, "Sensitivity analysis of the seismic performance of existing masonry buildings," *Engineering Structures*, vol. 80, pp. 137–146, 2014.
45. P. Jäger, P. Steinmann, and E. Kuhl, "On local tracking algorithms for the simulation of three-dimensional discontinuities," *Computational Mechanics*, vol. 42, no. 3, pp. 395–406, 2008.
46. S.-N. Roth, P. Léger, and A. Soulaïmani, "A combined XFEM-damage mechanics approach for concrete crack propagation," *Computer Methods in Applied Mechanics and Engineering*, vol. 283, pp. 923–955, jan 2015.
47. Y. Zhang, R. Lackner, M. Zeiml, and H. a. Mang, "Strong discontinuity embedded approach with standard SOS formulation: Element formulation, energy-based crack-tracking strategy, and validations," *Computer Methods in Applied Mechanics and Engineering*, vol. 287, pp. 335–366, 2015.
48. S. Saloustros, L. Pelà, and M. Cervera, "A crack-tracking technique for localized cohesive-frictional damage," *Engineering Fracture Mechanics*, vol. 150, pp. 96–114, 2015.
49. L. Pelà, M. Cervera, S. Oller, and M. Chiumenti, "A localized mapped damage model for orthotropic materials," *Engineering Fracture Mechanics*, vol. 124-125, pp. 196–216, 2014.
50. C. Linder and A. Raina, "A strong discontinuity approach on multiple levels to model solids at failure," *Computer Methods in Applied Mechanics and Engineering*, vol. 253, pp. 558–583, 2013.
51. M. H. Motamedi, D. A. Weed, and C. D. Foster, "Numerical simulation of mixed mode (I and II) fracture behavior of pre-cracked rock using the strong discontinuity approach," *International Journal of Solids and Structures*, vol. 85-86, pp. 44–56, 2016.
52. J.-b. Li, X.-a. Fu, B.-b. Chen, C. Wu, and G. Lin, "Modeling crack propagation with the extended scaled boundary finite element method based on the level set method," *Computers and Structures*, vol. 167, pp. 50–68, 2016.
53. J. Y. Wu, F. B. Li, and S. L. Xu, "Extended embedded finite elements with continuous displacement jumps for the modeling of localized failure in solids," *Computer Methods in Applied Mechanics and Engineering*, vol. 285, pp. 346–378, 2015.
54. S. Feld-Payet, V. Chiaruttini, J. Besson, and F. Feyel, "A new marching ridges algorithm for crack path tracking in regularized media," *International Journal of Solids and Structures*, vol. 71, pp. 57–69, 2015.
55. C. Comi and U. Perego, "Fracture energy based bi-dissipative damage model for concrete," *International Journal Of Solids And Structures*, vol. 38, no. 36-37, pp. 6427–6454, 2001.
56. L. Pelà, M. Cervera, and P. Roca, "Continuum damage model for orthotropic materials: Application to masonry," *Computer Methods in Applied Mechanics and Engineering*, vol. 200, pp. 917–930, feb 2011.
57. G. Z. Voyiadjis, Z. N. Taqieddin, and P. I. Kattan, "Theoretical Formulation of a Coupled Elastic–Plastic Anisotropic Damage Model for Concrete using the Strain Energy Equivalence Concept," *International Journal of Damage Mechanics*, vol. 18, no. 7, pp. 603–638, 2009.
58. J. Mazars, F. Hamon, and S. Grange, "A new 3D damage model for concrete under monotonic, cyclic and dynamic loadings," *Materials and Structures*, pp. 3779–3793, 2014.
59. W. He, Y. F. Wu, Y. Xu, and T. T. Fu, "A thermodynamically consistent nonlocal damage model for concrete materials with unilateral effects," *Computer Methods in Applied Mechanics and Engineering*, vol. 297, pp. 371–391, 2015.
60. L. F. Pereira, J. Weerheijm, and L. J. Sluys, "A new rate-dependent stress-based nonlocal damage model to simulate dynamic tensile failure of quasi-brittle materials," *International Journal of Impact Engineering*, vol. 94, pp. 83–95, 2016.
61. J. Lemaitre and J. L. Chaboche, "Aspect Phenomenologique de la Rupture par Endommagement," *Journal de Mécanique Appliquée*, vol. 2, no. 3, 1978.
62. J. C. Simo and J. W. Ju, "Strain- and stress-based continuum damage models-I. Formulation," *International Journal of Solids and Structures*, vol. 23, no. 7, pp. 821–840, 1987.
63. J. Oliver, M. Cervera, S. H. Oller Martinez, and J. Lubliner, "Isotropic damage models and smeared crack analysis of concrete," *Proc. SCI-C Computer Aided Analysis and Design of Concrete Structures*, no. February, pp. 945–957, 1990.

64. Z. Bazant and B. Oh, "Crack band theory for fracture of concrete," *Materials and Structures*, vol. 16, pp. 155–177, 1983.
65. M. Cervera, "Viscoelasticity and Rate-dependent Continuum Damage Models, Monography N-79," tech. rep., Barcelona, 2003.
66. J. Oliver, "A consistent characteristic length for smeared cracking models," *International Journal for Numerical Methods in Engineering*, vol. 28, no. 2, pp. 461–474, 1989.
67. J.-Y. Wu and M. Cervera, "On the equivalence between traction- and stress-based approaches for the modeling of localized failure in solids," *Journal of the Mechanics and Physics of Solids*, vol. 82, pp. 137–163, 2015.
68. M. Cervera and J.-Y. Wu, "On the conformity of strong, regularized, embedded and smeared discontinuity approaches for the modeling of localized failure in solids," *International Journal of Solids and Structures*, vol. 71, pp. 19–38, 2015.
69. ASTM:C496/C496M, "Standard Test Method for Splitting Tensile Strength of Cylindrical Concrete Specimens," *ASTM International*, no. 336, pp. 1–5, 2011.
70. ASTM:D3967-08, "Standard Test Method for Splitting Tensile Strength of Intact Rock Core Specimens," *ASTM International*, 2008.
71. COMET, "Coupled Mechanical and Thermal analysis, http://www.cimne.com/comet/," 2013.
72. GiD, "The personal pre and post-processor, http://www.gidhome.com/," 2014.
73. EN 1992 (Eurocode 2), "Design of concrete structures," tech. rep., London, 1992.
74. N. Augenti, F. Parisi, A. Prota, and G. Manfredi, "In-Plane Lateral Response of a Full-Scale Masonry Subassemblage with and without an Inorganic Matrix-Grid Strengthening System," *Journal of Composites for Construction*, vol. 15, no. 4, pp. 578–590, 2011.
75. F. Parisi, G. P. Lignola, N. Augenti, a. Prota, and G. Manfredi, "Nonlinear Behavior of a Masonry Subassemblage Before and After Strengthening with Inorganic Matrix-Grid Composites," *Journal of Composites for Construction*, vol. 15, no. 5, pp. 821–832, 2011.
76. EN 1998-1 (Eurocode 8), "Design of structures for earthquake resistance, Part 1 General rules seismic actions and rules for buildings," 2003.
77. P. Fajfar, "Capacity spectrum method based on inelastic demand spectra," *Earthquake Engineering & Structural Dynamics*, vol. 28, pp. 979–993, sep 1999.